

The key role of bedrock composition in the formation of carbonates on Mars

C. Gil-Lozano, F. Baron, A. Gaudin, J.-P. Lorand, V. Fernandez,
J. Hamon, N. Mangold

Supplementary Information

The Supplementary Information includes:

- Materials and Methods
- Table S-1
- Figures S-1 to S-8
- Geochemical Modelling and Carbonates
- Supplementary Information References

Materials and methods

Starting materials and experimental set-up. As starting minerals we chose a list of individual minerals, namely forsterite – magnesium and iron-rich-, clinopyroxene, plagioclase, and potassium feldspar, as well as two prepared martian crust simulants constrained by the early Mars crust composition inferred by the conglomerate analysed in the Gale crater (Mangold *et al.*, 2016) and the Martian regolith breccia NWA 7533 and NWA 7034 (Agee *et al.*, 2013; Humayun *et al.*, 2013; Hewins *et al.*, 2017) (Table 1). These martian crust simulants were built by a mixture of individual minerals. This procedure allowed us to increase the dissolution rate of silicate minerals under low temperature conditions. The bulk chemical composition of Mars simulants samples was estimated according to the proportion of the minerals (wt. % in Table 1). Both Mars crust simulants present a high proportion of K-feldspars to balance the low Na-content of plagioclase and fit the alkali-rich composition of martian regolith breccias. Specifically, in a total alkali-silica (TAS) diagram (Le Bas *et al.*, 1986) the chemical composition of simulant containing Fo₆₅-olivine (Sim-O) is consistent with basaltic andesite, whereas the simulant containing magnetite but lacking olivine (Sim-M), with high Fe content fits better with a basaltic composition. Each mineral was crushed, sieved ($\varnothing < 63 \mu\text{m}$) and settled in ethanol to remove the fine fraction ($\varnothing < 2 \mu\text{m}$).

Aqueous alteration experiments reproducing martian weathering under a thick CO₂ atmosphere were performed under a controlled anoxic CO₂ atmosphere (*i.e.* Mbraun-LABstar glovebox with a constant pCO₂ = 1 bar, Air Liquide® Alphagaz CO₂) for 6 months (Baron *et al.*, 2019) (Fig. S-1). The O₂ concentration was continuously monitored with an oxygen analyser (MB-OX-EC-PLC, over the 1- to 1000 ppm range) and kept below pO₂ < 0.5 ppm by a gas purification unit. The samples were placed into batch Savillex™ PFA reactors (90 mL– references 100-0090-01 for the reactor and 600-053-20 for the closure) (containing 1.8 g of starting material and 18 mL of ultrapure water, 18 MΩ cm) and allowed

to react in closed conditions at a relatively low water-to-rock ratio (W/R ~10 by weight). Milli-Q® ultrapure water (18 MΩ cm) was previously degassed three times under vacuum for 3 hours each time and then equilibrated under continuous stirring for 2 days with 1 atm of CO₂. The batch reactors were kept under continuous stirring (50 rpm using an orbital agitator) and at 45 °C (thermostatic hot plate) to increase the reaction rate. Initial pH values of anoxic ultrapure water were measured after 2 days of stirring conditions inside the glovebox to ensure equilibrium with pCO₂ = 1 bar atmosphere (pH₀ = 3.6). The final pH values of each experimental solution were measured at the end of the experiments in contact with minerals at 25 °C. The pH values were then estimated at 45 °C for each experimental solution from thermodynamic calculations. The calculations were performed using the PHREEQC® software (Parkhurst and Apello, 2014) associated with the Thermoddem database (<http://thermoddem.brgm.fr/>), further details concerning the sample preparation and experimental design can be found in Baron *et al.* (2019).

After 6 months of reaction, the samples were filtered (< 0.2 μm) and dried inside the glovebox to separate the solid product from the solutions. The previous work of Baron *et al.* (2019) analysed the physicochemical parameters of the experimental solutions. Here, we analyse the carbonate in the solid products, but some information about fluid chemistry that helps us to discuss the results can be found in Figures S-7 and S-8.

Analytical techniques. The initial and altered samples were analysed with X-ray photoelectron spectroscopy (XPS), Fourier transforms infrared spectroscopy (FTIR), and Field Emission Gun Scanning Electron Microscope (FEG-SEM).

XPS analyses were performed using a Kratos Axis Nova spectrometer (Institut de Matériaux de Nantes, IMN, Nantes) equipped with a monochromatic Al-Kα (hν = 1486.6 eV) with a surface analysed of 700 μm x 300 μm. The base pressure of the system was below 10⁻⁹ mbar. Survey spectra were acquired by using 160 eV pass energy, whereas a 40 eV pass energy was applied for the analysis of the core level spectra (C1s, Si 2p, O1s, Mg 2p, and Fe2p). With the pass energy 160 eV and 40 eV, the all-over instrument resolution on the Fermi edge is about 1.9 eV and 0.56 eV, respectively. All data were acquired using charge compensation to establish a steady-state surface potential.

Mid-Infrared spectra (MIR: 4000-400 cm⁻¹) were collected using an FTIR-Nicolet 5700 spectrometer (LPG, Nantes), using a DTGS KBr detector, and a KBr beamsplitter at 4 cm⁻¹ resolution. All spectra correspond to an addition of 100 scans. The analyses were carried out on the bulk samples (*i.e.*, whole size fractions) and the finest fraction (particle size <1 μm) of the reacted samples. This fine fraction was extracted by the sedimentation method based on Stokes' law in ultrapure water (18 MΩ cm) inside the glovebox, subsequently filtered (< 0.2 μm), and allowed to dry under the controlled CO₂ atmosphere. Then, it was dispersed in a KBr matrix and measured under room conditions.

Field Emission Gun Scanning Electron Microscope (FEG-SEM) images were acquired using a JEOL JSM 7600F scanning electron microscope equipped with an Energy Dispersive Spectrometer (EDS) (IMN, Nantes).

Processing XPS data. XPS spectra were referenced to the C1s peak at 284.8 eV and analysed using CasaXPS software (version 2.3.24rev1.0R) (Fairley *et al.*, 2021). The XPS survey spectra provide information on the chemical composition of the samples (Fig. S-1), whereas C1s spectra provide the chemical composition of the carbon species. We focused on the C1s high-resolution spectra for carbonate species because the O1s orbitals are hard to deconvolve due to the presence of several oxygen-bearing species (*i.e.*, oxides, hydroxides, silicates, carbonates) and can occur within a narrow range of binding energies (Kloprogge and Wood, 2020). In the C1s spectra, all the samples present the usual contribution of ubiquitous adventitious carbon due to the physisorption of hydrocarbon layers from both the exposure to the atmosphere and the vacuum system of the instrument (Cánneva *et al.*, 2017; Kloprogge and Wood, 2020). We performed a curve fitting of the C1s high-resolution spectra to determine the amount of the carbonate component in the samples using reported literature values (Payne *et al.*, 2011; Kloprogge and Wood, 2020). The fit was performed with fixed components positions resulting in good FWHM homogeneity (Fig. 1, Fig. S-2, and Table S-1). Specifically, we used four components for the ubiquitous hydrocarbon species (Payne *et al.*, 2011): C-C/C-H (284.8 ± 0.1 eV); C-O (286.1 ± 0.1 eV); C=O (287.7 ± 0.1 eV) and O-C=O (288.7 ± 0.1 eV); whereas the carbonate component position was assigned with higher deviation (289.7 ± 0.4 eV) because it depends on the ionic character of the metal-carbon bond (*e.g.*, MgCO₃ ~ 290 eV and CaCO₃/FeCO₃ ~ 289.5 eV) (Kloprogge and Wood, 2020). We used a Voigt line Lorentzian Asymmetric (LA) function for the line shape and a U 2 Tougaard function for the background. Individual peak parameters of the fitting



can be found in Table S-1. To obtain a comprehensive overview of the total amount of the surface carbonates formed (Fig. 2), we normalised the percentages of carbonate species from the high-resolution spectra (Table S-1) to the total carbon content on the surface estimated from the survey spectra (Fig. S-1). Then, we subtracted the contribution of hydrocarbon adventitious species and the oxygen component related to them using the calculator described by Payne *et al.* (2011) and recalculated the % of the carbonate component.



Supplementary Tables

Table S-1 Individual peak parameters identified in the fitting of the C1s high-resolution spectra for iron-rich olivine (Fo₆₅-olivine), magnesium-rich olivine (Fo₉₂-olivine), clinopyroxene (cpx), potassium-feldspar (k-spar), plagioclase (PLA), simulant with olivine (Sim-O) and simulant with magnetite (Sim-M) (Fig. 1 and extended Fig. S-2)

Fo₆₅-olivine initial (residual STD=1.06)

| Name | Position | FWHM | %Con. |
|-----------------|----------|------|-------|
| C-C, C-H | 284.8 | 1.5 | 75.2 |
| C-O | 286.2 | 1.5 | 13.8 |
| C=O | 287.8 | 1.5 | 1.5 |
| O-C=O | 288.8 | 1.5 | 7.3 |
| CO ₃ | 289.9 | 1.4 | 2.2 |

Fo₆₅-olivine reacted (CO₂ atm) (residual STD=0.80)

| Name | Position | FWHM | %Con. |
|-----------------|----------|------|-------|
| C-C, C-H | 284.8 | 1.6 | 63.1 |
| C-O | 286.2 | 1.6 | 14.0 |
| C=O | 287.7 | 1.6 | 3.6 |
| O-C=O | 288.7 | 1.6 | 1.9 |
| CO ₃ | 290.1 | 2.0 | 17.4 |

Fo₉₂-olivine initial (residual STD= 1.15)

| Name | Position | FWHM | %Con. |
|-----------------|----------|------|-------|
| C-C, C-H | 284.8 | 1.6 | 72.1 |
| C-O | 286.2 | 1.6 | 16.2 |
| C=O | 287.6 | 1.6 | 1.9 |
| O-C=O | 288.8 | 1.6 | 7.6 |
| CO ₃ | 289.9 | 1.6 | 2.2 |

Fo₉₂-olivine reacted (CO₂ atm) (residual STD=1.02)

| Name | Position | FWHM | %Con. |
|-----------------|----------|------|-------|
| C-C, C-H | 284.8 | 1.6 | 64.9 |
| C-O | 286.3 | 1.6 | 15.3 |
| C=O | 287.6 | 1.6 | 3.7 |
| O-C=O | 288.6 | 1.6 | 1.7 |
| CO ₃ | 290.1 | 2.1 | 14.5 |

Cpx initial (residual STD=0.95)

Cpx reacted (CO₂ atm) (residual STD=1.34)

| Name | Position | FWHM | %Con. |
|-----------------|----------|------|-------|
| C-C, C-H | 284.8 | 1.6 | 66.3 |
| C-O | 286.1 | 1.6 | 21.0 |
| C=O | 287.6 | 1.6 | 4.6 |
| O-C=O | 288.8 | 1.6 | 3.5 |
| CO ₃ | 289.7 | 2.0 | 4.6 |

| Name | Position | FWHM | %Con. |
|-----------------|----------|------|-------|
| C-C, C-H | 284.8 | 1.6 | 75.4 |
| C-O | 286.2 | 1.6 | 14.6 |
| C=O | 287.6 | 1.6 | 2.1 |
| O-C=O | 288.8 | 1.6 | 5.1 |
| CO ₃ | 289.4 | 1.4 | 2.8 |

K-spar initial (residual STD=0.94)

K-spar reacted (CO₂ atm) (residual STD=1.33)

| Name | Position | FWHM | %Con. |
|----------|----------|------|-------|
| C-C, C-H | 284.8 | 1.5 | 91.0 |
| C-O | 286.1 | 1.5 | 8.7 |
| C=O | 287.6 | 1.5 | 0.3 |
| O-C=O | 288.8 | 1.5 | 0.0 |

| Name | Position | FWHM | %Con. |
|----------|----------|------|-------|
| C-C, C-H | 284.8 | 1.6 | 83.4 |
| C-O | 286.1 | 1.6 | 15.2 |
| C=O | 287.6 | 1.6 | 1.4 |
| O-C=O | 288.7 | 1.6 | 0.0 |

Pla initial (residual STD=1.33)

| Name | Position | FWHM | %Con. |
|-----------------|----------|------|-------|
| C-C, C-H | 284.8 | 1.6 | 73.9 |
| C-O | 286.1 | 1.6 | 18.5 |
| C=O | 287.6 | 1.6 | 2.6 |
| O-C=O | 288.8 | 1.6 | 2.3 |
| CO ₃ | 289.5 | 1.8 | 2.7 |

Pla reacted (CO₂ atm) (residual STD=1.02)

| Name | Position | FWHM | %Con. |
|-----------------|----------|------|-------|
| C-C, C-H | 284.8 | 1.5 | 74.3 |
| C-O | 286.1 | 1.5 | 15.8 |
| C=O | 287.6 | 1.5 | 3.2 |
| O-C=O | 288.8 | 1.5 | 2.1 |
| CO ₃ | 289.5 | 1.7 | 4.6 |



Sim-O initial (residual STD=1.55)

| Name | Position | FWHM | %Con. |
|-----------------|----------|------|-------|
| C-C, C-H | 284.8 | 1.6 | 69.2 |
| C-O | 286.2 | 1.6 | 21.7 |
| C=O | 287.8 | 1.6 | 3.1 |
| O-C=O | 288.6 | 1.6 | 2.7 |
| CO ₃ | 289.4 | 1.8 | 3.3 |

Sim-O reacted (CO₂ atm) (residual STD=1.71)

| Name | Position | FWHM | %Con. |
|-----------------|----------|------|-------|
| C-C, C-H | 284.8 | 1.6 | 69.0 |
| C-O | 286.2 | 1.6 | 22.2 |
| C=O | 287.8 | 1.6 | 3.4 |
| O-C=O | 288.8 | 1.6 | 0.9 |
| CO ₃ | 289.4 | 1.9 | 4.5 |

Sim-M initial (residual STD=1.34)

| Name | Position | FWHM | %Con. |
|-----------------|----------|------|-------|
| C-C, C-H | 284.8 | 1.6 | 72.6 |
| C-O | 286.2 | 1.6 | 20.1 |
| C=O | 287.8 | 1.6 | 3.0 |
| O-C=O | 288.8 | 1.6 | 1.3 |
| CO ₃ | 289.4 | 1.8 | 3.1 |

Sim-M reacted (CO₂ atm) (residual STD=2.44)

| Name | Position | FWHM | %Con. |
|-----------------|----------|------|-------|
| C-C, C-H | 284.8 | 1.6 | 69.9 |
| C-O | 286.2 | 1.6 | 22.1 |
| C=O | 287.8 | 1.6 | 2.9 |
| O-C=O | 288.6 | 1.6 | 0.3 |
| CO ₃ | 289.5 | 1.9 | 4.8 |



Supplementary Figures

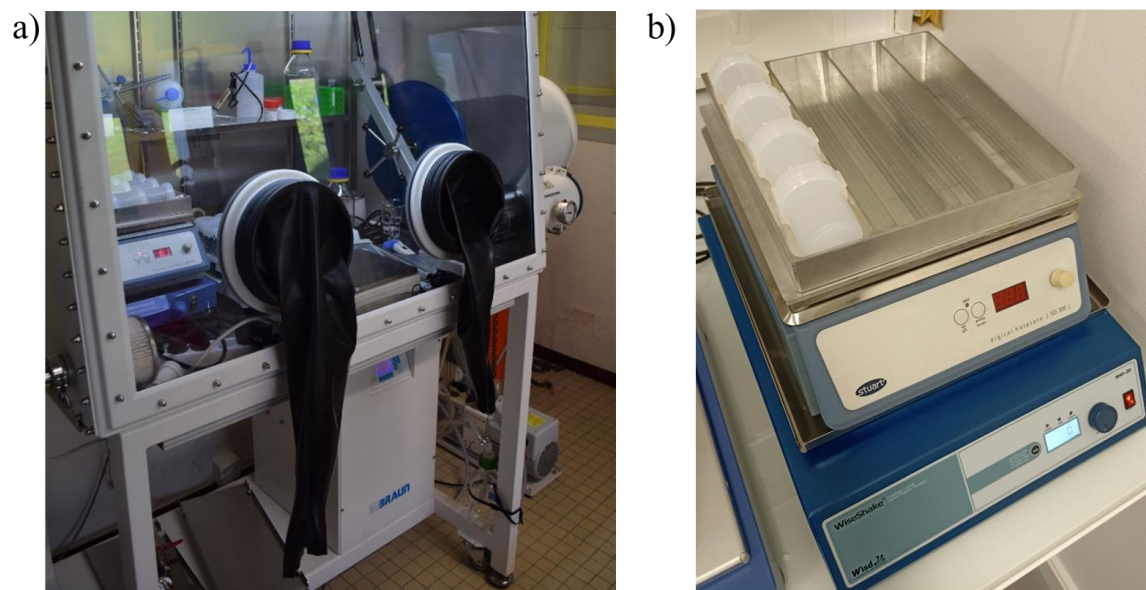
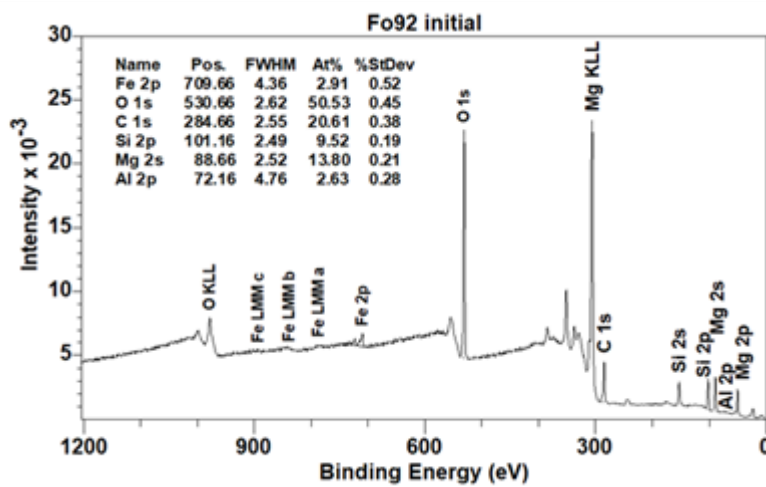
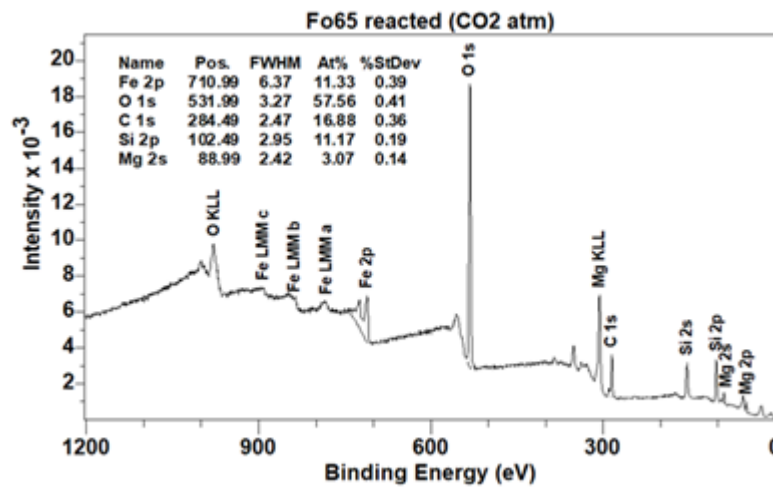
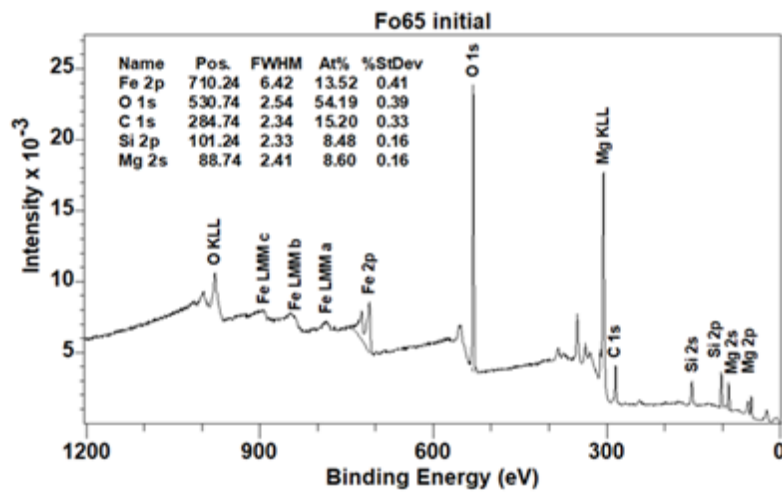
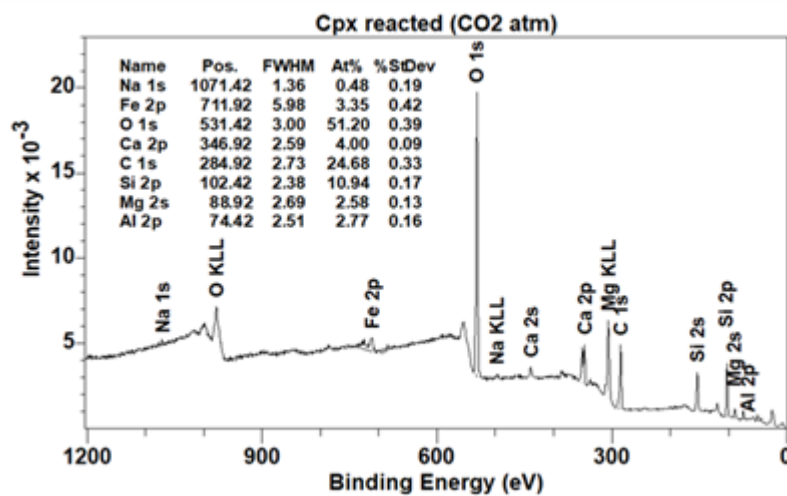
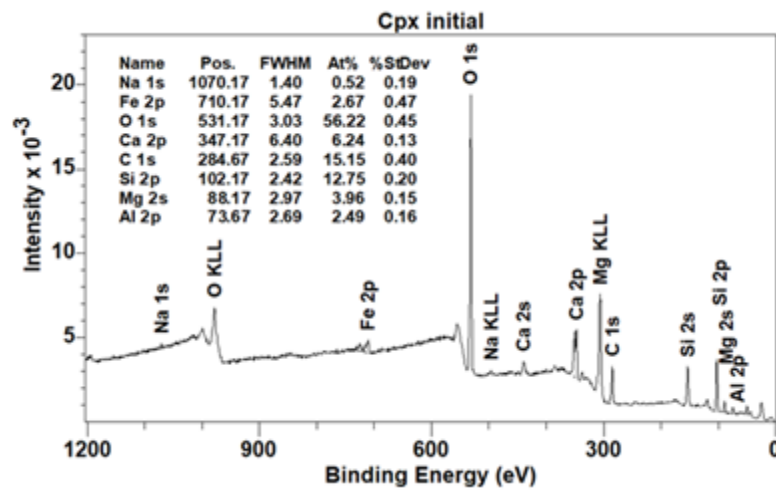
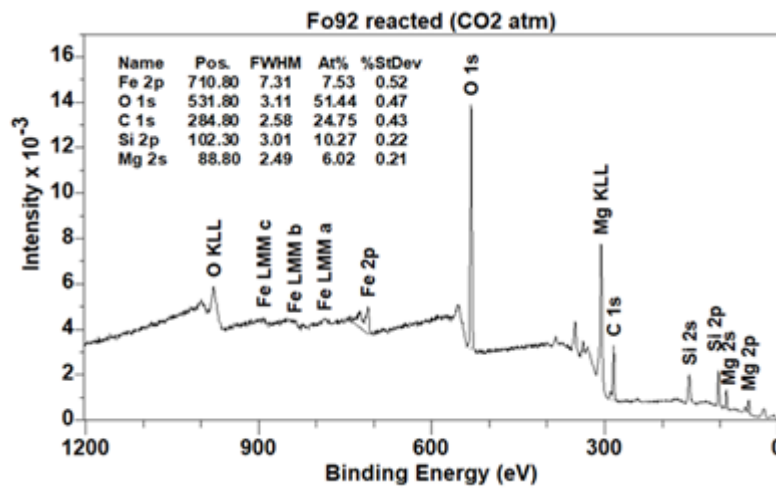
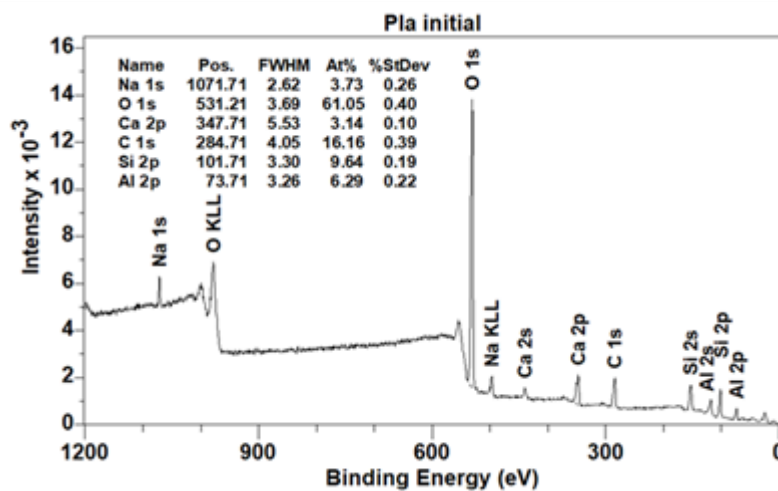
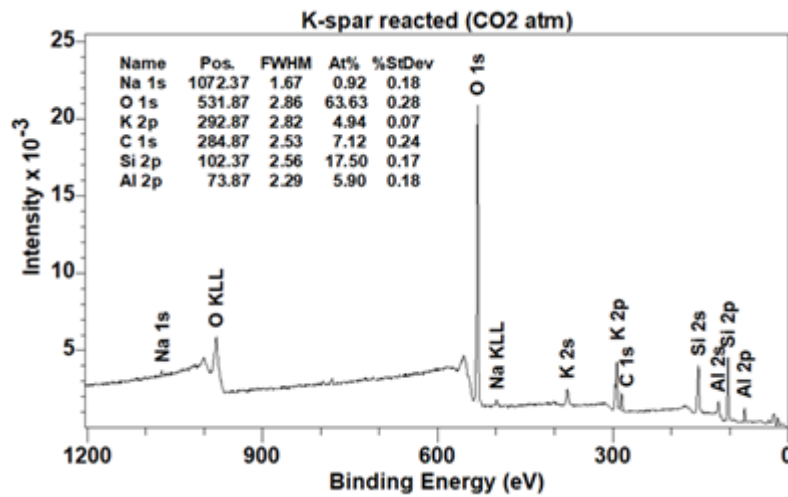
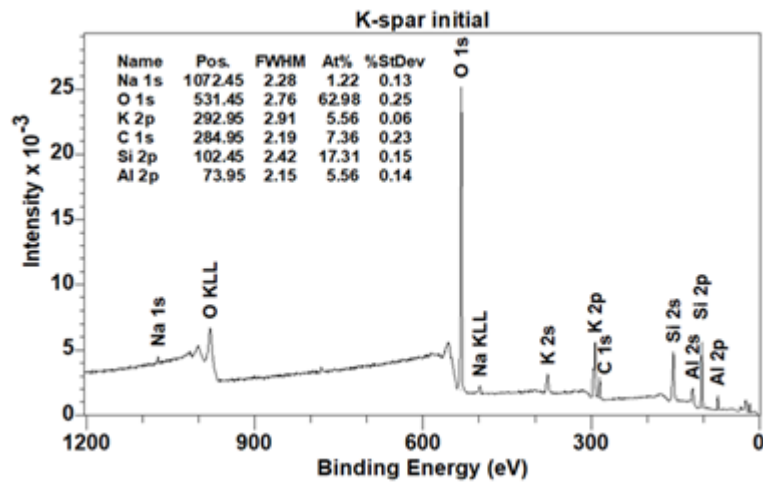
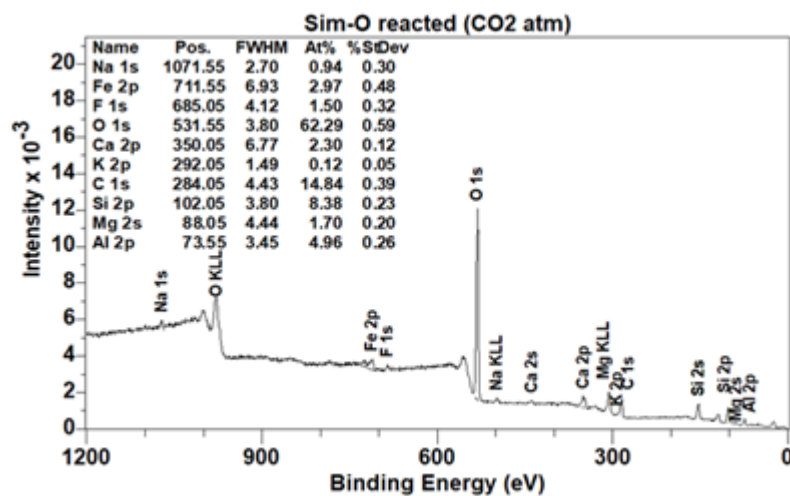
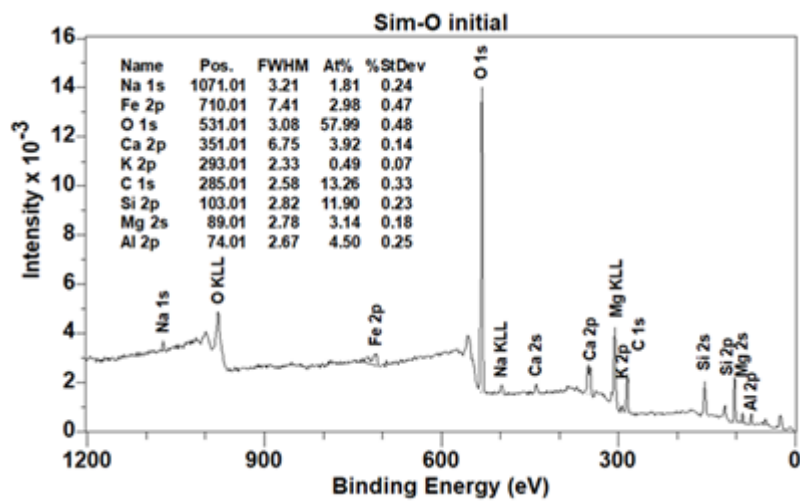
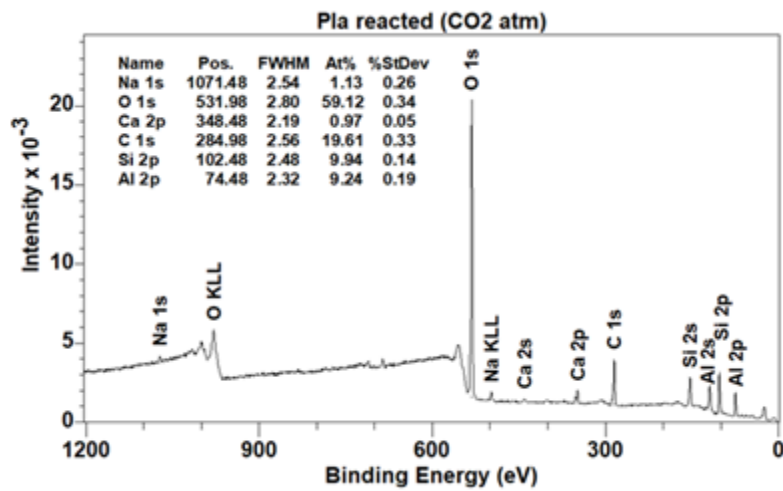


Figure S-1 (a) Picture of the experiment running in the glovebox. (b) Picture of the reactors, showing from down to top: stirring plate, hot plate and, an aluminium sample holder for the heat conductivity.









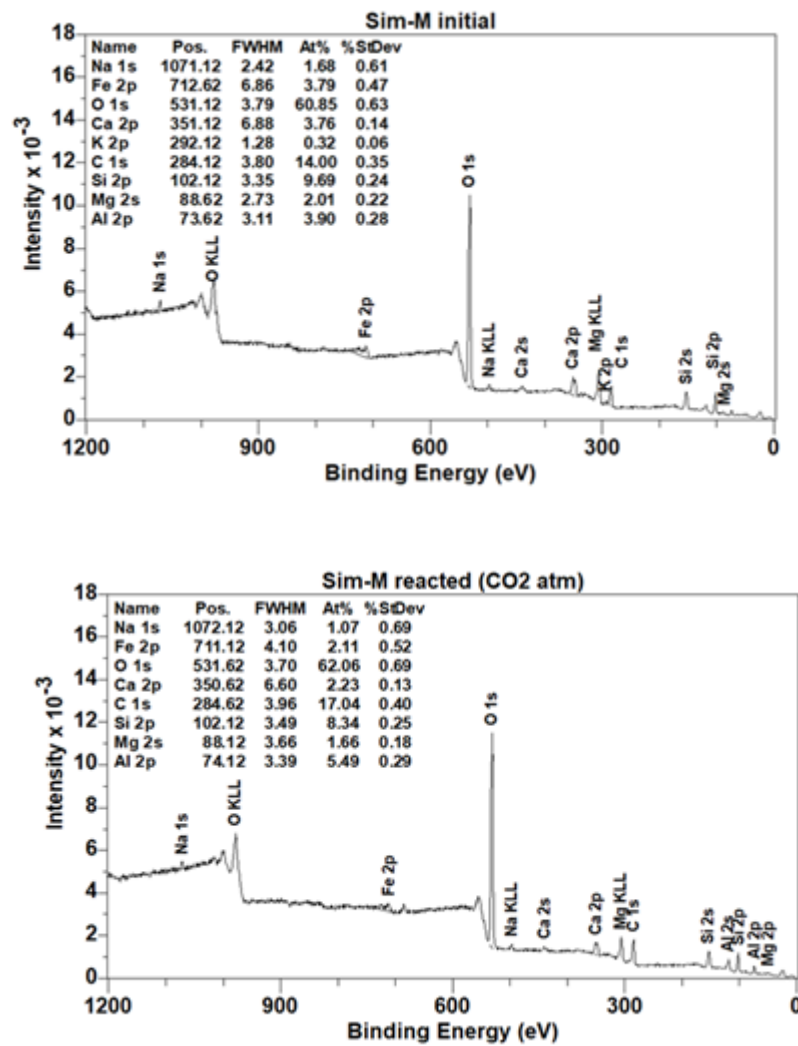
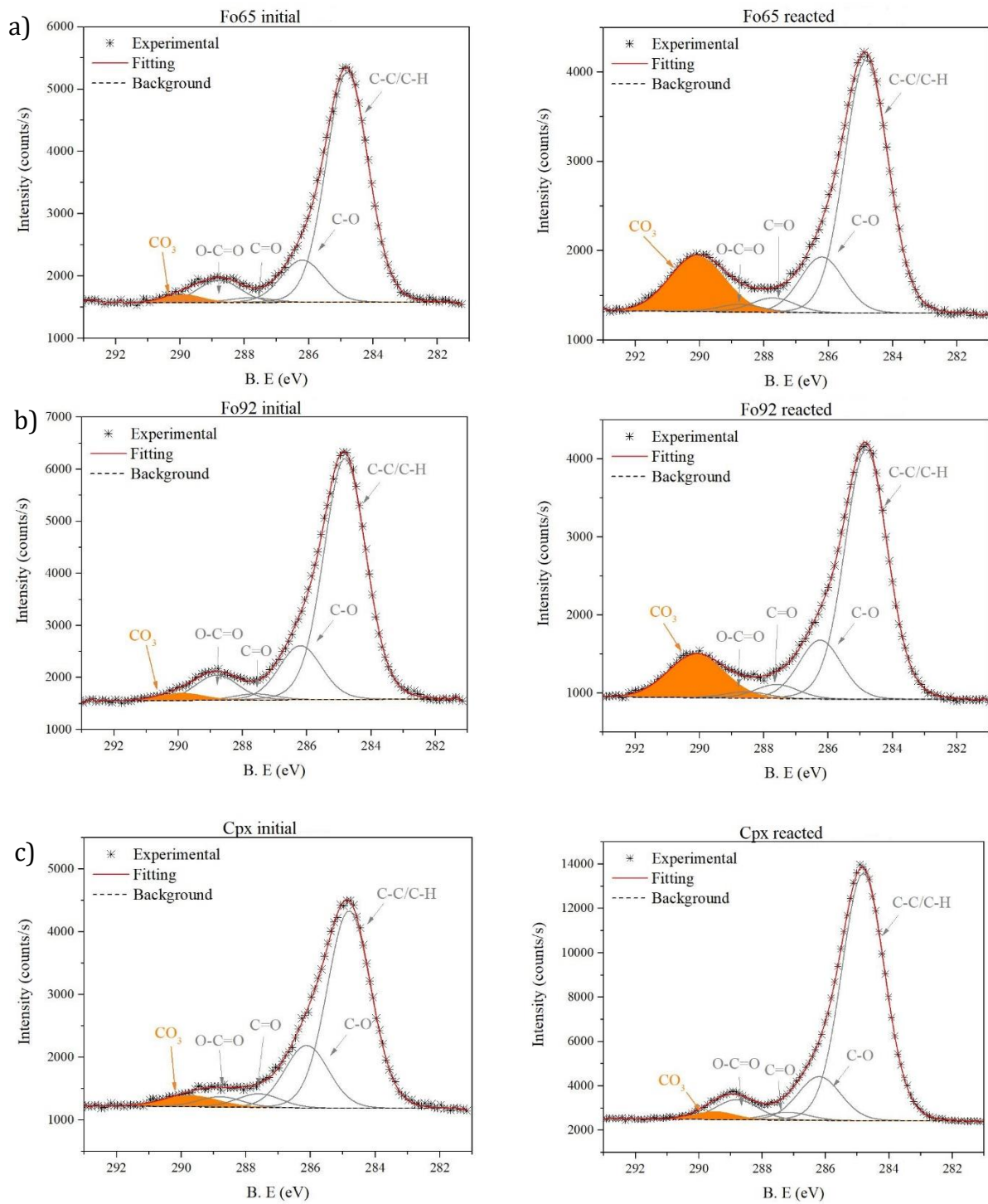
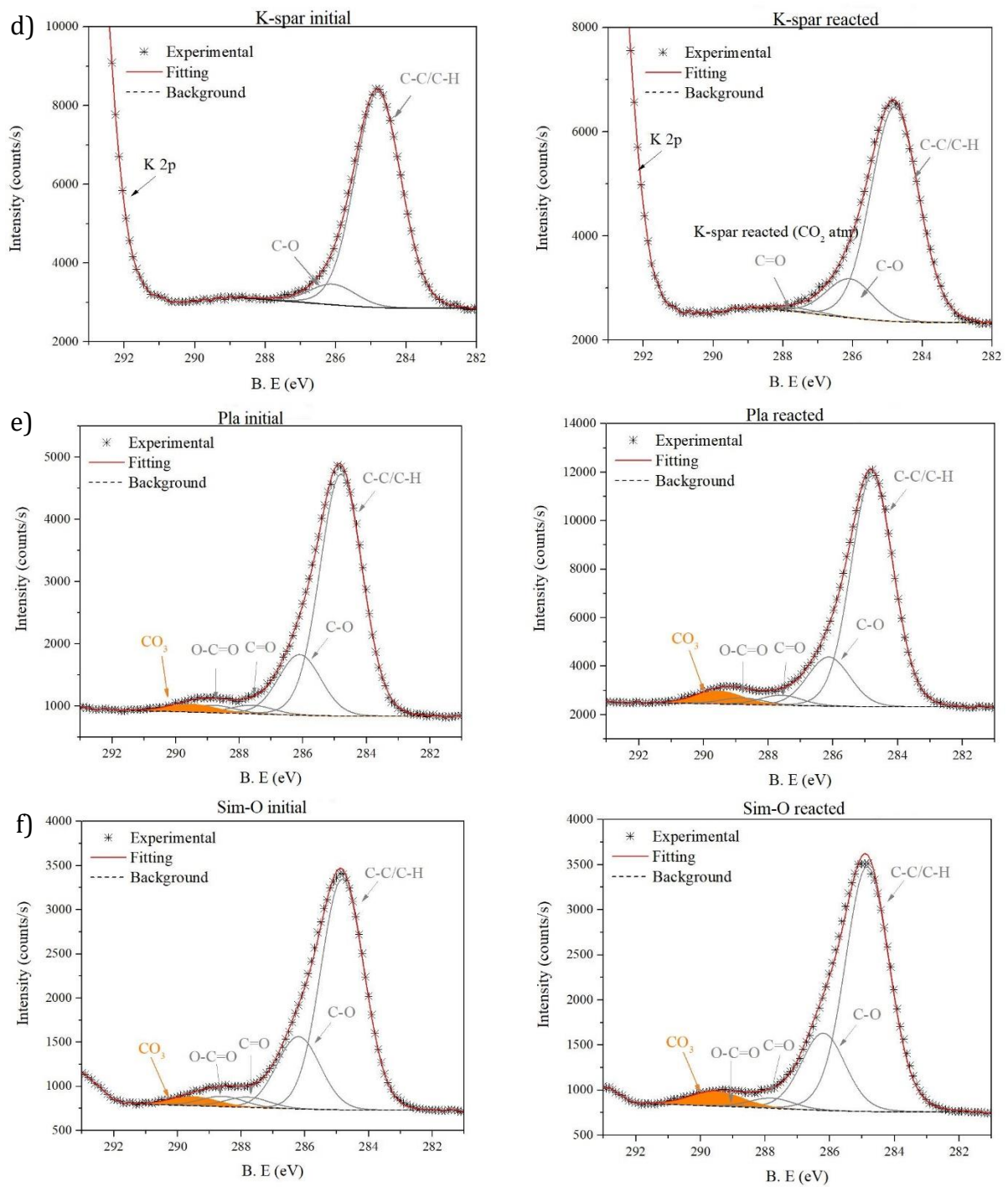


Figure S-2 Quantification of XPS survey spectra from the samples analysed in this study. From the top to the bottom, initial (before reaction) and reacted (after aqueous alteration under pCO₂): Fo₆₅-olivine (Fo₆₅); Fo₉₂-olivine (Fo₉₂); augite (Cpx); K-feldspar (K-spar); anorthite (Pla); simulant-O (Sim-O); simulant-M (Sim-M).





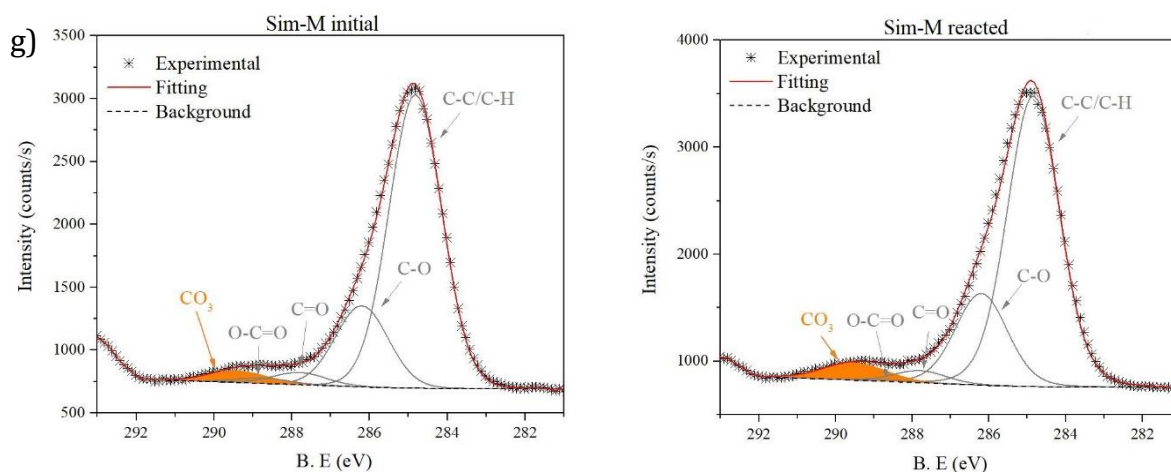


Figure S-3 Fitting model of high-resolution C1s spectra to identify adventitious carbon (grey) and carbonate species (orange). Individual peak parameters are shown in Table S.1. The left column shows the initial samples and the right the reacted samples under a CO₂ atmosphere: **(a)** Fo₆₅-olivine (Fo₆₅), **(b)** Fo₉₂-olivine (Fo₉₂), **(c)** clinopyroxene (Cpx), **(d)** potassium feldspar (K-spar), **(e)** plagioclase (Pla), **(f)** Mars crust simulant-O (Sim-O) and, **(g)** Mars crust simulant-M (Sim-M).

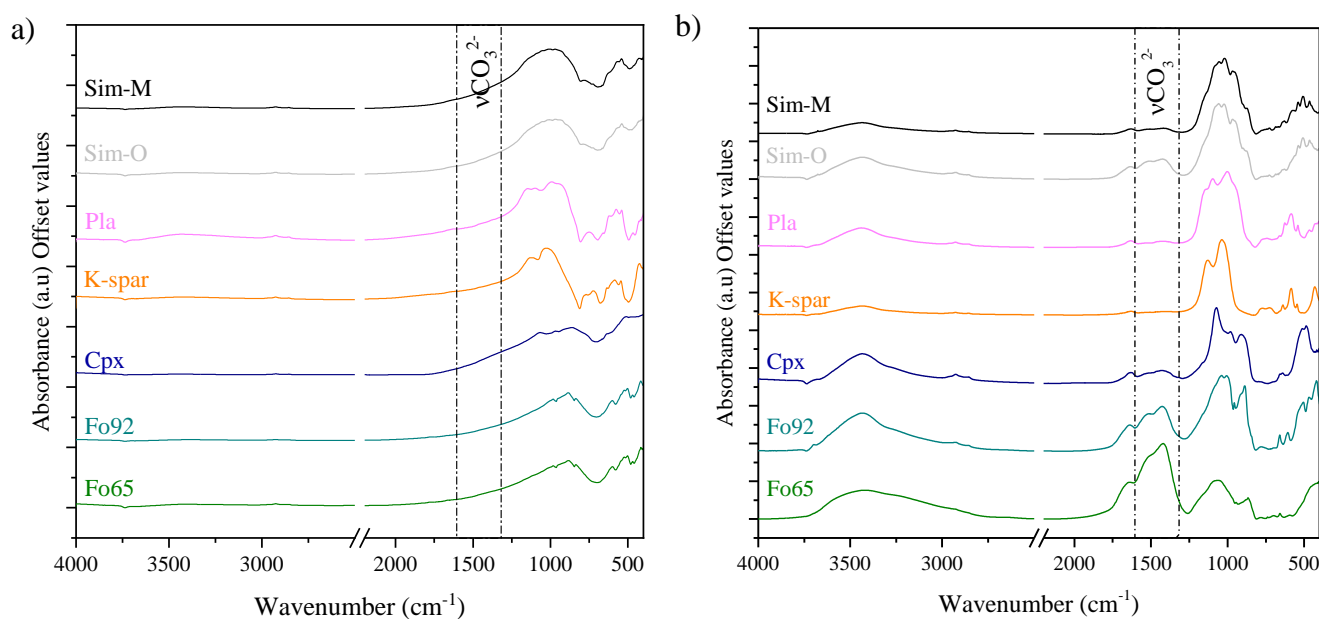


Figure S-4 Mid-IR spectra of reacted samples: **(a)** bulk samples, **(b)** size fraction <1 μm. From the bottom to the top: Fo₆₅-olivine (Fo₆₅), Fo₉₂-olivine (Fo₉₂), clinopyroxene (Cpx), K-feldspar (K-spar), plagioclase (Pla), simulant-O (Sim-O), and simulant-M (Sim-M). Dashed lines mark the region of the asymmetric stretching vibration of the carbonates group ($\nu_3(\text{CO}_3)^{2-}$) (Jones and Jackson, 1993).



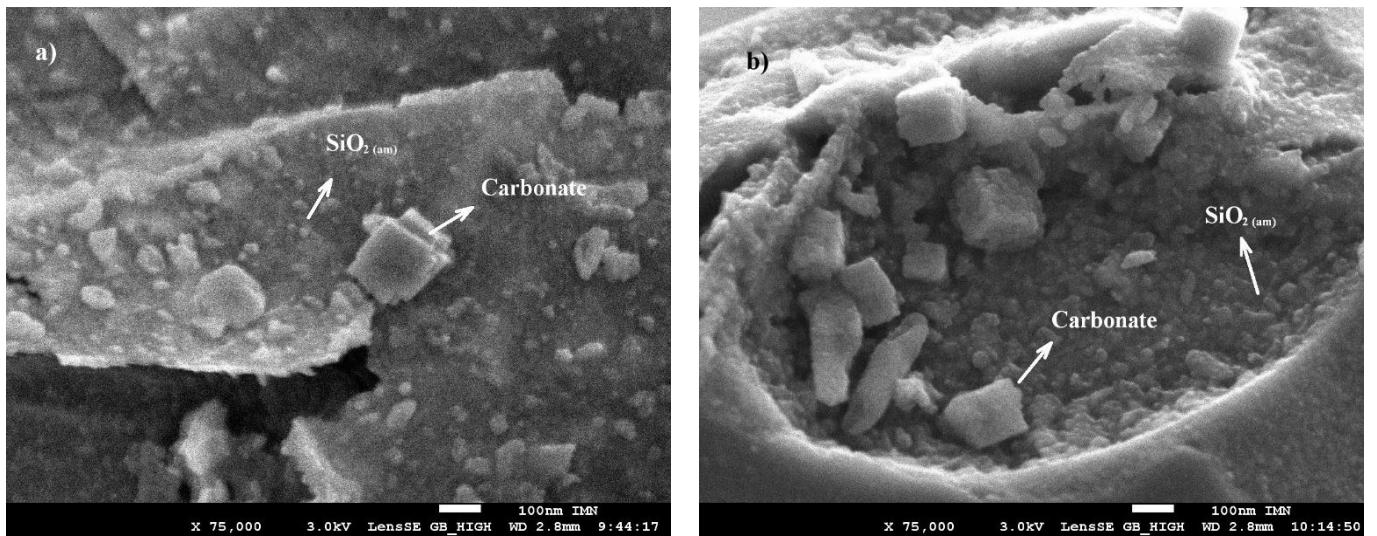


Figure S-5 FG-SEM images of Fo₆₅-olivine reacted sample.

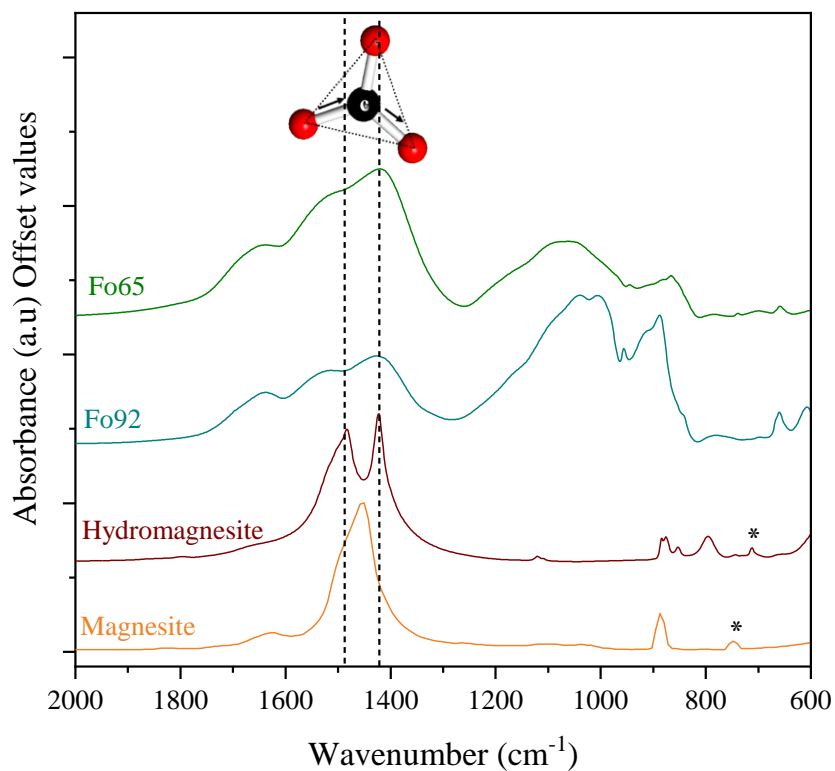


Figure S-6 IR-spectra in the 2000-600 cm^{-1} region of the finest fraction (particle size $< 1 \mu\text{m}$) of olivine-weathered samples (Fo₆₅ and Fo₉₂) on the top and, hydromagnesite and magnesite spectra on the bottom for comparison (from HR inorganics Thermo Fisher database). The split band of asymmetric stretching bands of carbonates ($\nu_3(\text{CO}_3)^{2-}$) matches better with hydromagnesite (dashed lines) than with the magnesite spectrum. The asterisks mark the symmetric band $\nu_4(\text{CO}_3)^{2-}$, which only appears in crystalline carbonate (Gago-Duport *et al.*, 2008).

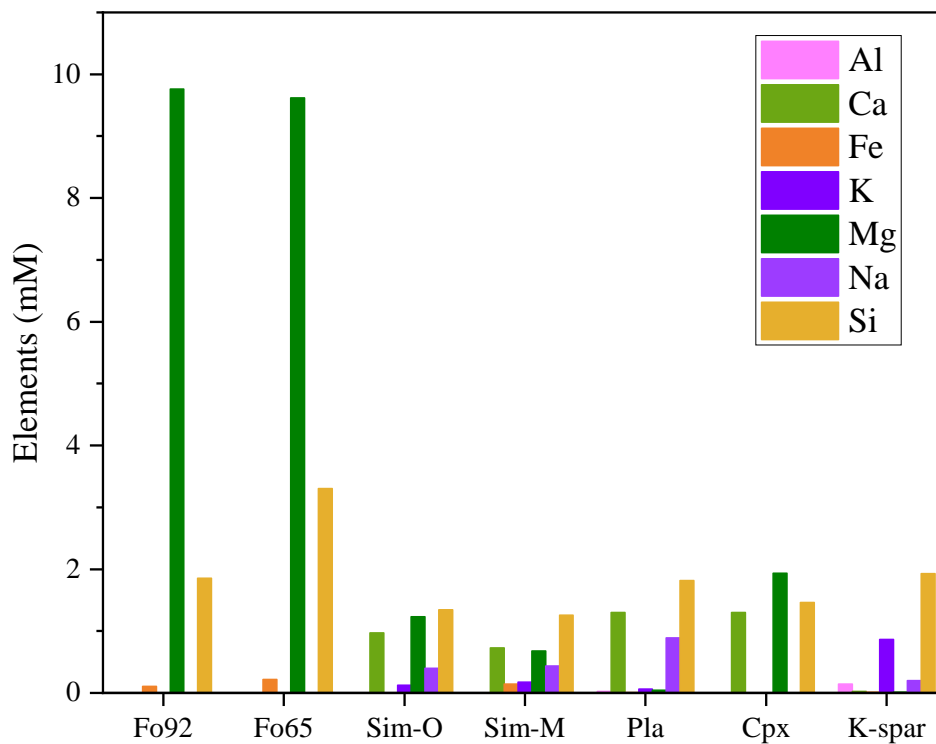


Figure S-7 The fluid chemistry of the samples: magnesium forsterite (Fo₉₂); ferroan forsterite (Fo₆₅), simulant with olivine (Sim-O); simulant with magnetite (Sim-M); plagioclase (Pla); clinopyroxene (Cpx); K-feldspar (K-spar). They were analysed by Baron *et al.* (2019) using inductively coupled plasma atomic emission spectroscopy (ICP-AES).

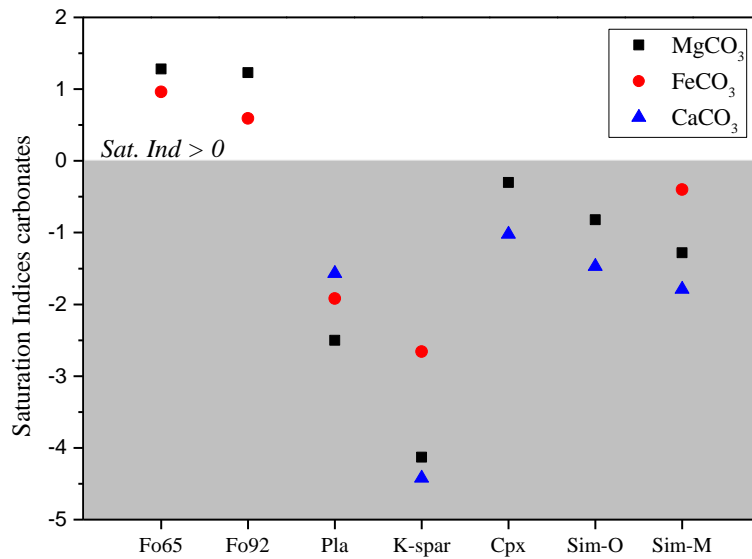


Figure S-8 Mineral saturation indices of carbonates were calculated by Baron *et al.* (2019) with the Phreeqc software and the Thermoddem database. The Eh-pH predominance diagrams of iron solutions showed that olivine reacted samples yielded oxidising conditions that inhibit the formation of siderite.

➤ Geochemical Modelling and Carbonates

The geochemical models considering equilibrium conditions might lead to some uncertainties about the secondary products formed. In these models, a mineral phase can instantaneously precipitate or dissolve, depending on its saturation index (SI), Equation S-1:

$$SI = \log \left(\frac{IAP}{K_{sp}} \right) \quad \text{Eq. S-1}$$

Being IAP, the ionic activity product of the chemical species, and K_{sp} the solubility product of the mineral. Accordingly, $SI > 0$ indicates mineral precipitation, and $SI < 0$, mineral dissolution.

However, equilibrium calculations are usually biased by the mineral assemblage chosen in the input file, having a significant impact on the model results (Dethlefsen *et al.*, 2012). Additionally, previous studies with batch reactor experiments have shown a strong coupling between mineral dissolution/precipitation kinetic reactions, and consequently, equilibrium conditions were not attained (Zhu and Lu, 2009; Lu *et al.*, 2013). In this regard, it is important to mention the role of metastable phases, usually not considered in equilibrium models, which are essential to determine the growth of carbonates (Montes-Hernandez and Renard, 2016). Another issue is the effect of secondary ions on the formation of carbonates, such as the well-known inhibition effect of the Mg^{2+} or SO_4^{2-} ions over calcite formation (*e.g.*, Nielsen *et al.*, 2016).

More challenging is to adapt the macroscopic rate laws (*i.e.* that are based upon the chemical affinity of bulk experiments) to incorporate surface microscopic processes (Teng *et al.*, 2000), including the dependence on the degree of supersaturation to overcome the nucleation processes and begin crystal growth (Jiang and Tosca, 2020; Kissick *et al.*, 2021).

For these reasons, geochemical models from basalt dissolution on early Mars might overestimate the carbonate formation. Thus, more laboratory experiments are necessary to refine geochemical models and adjust kinetic rates.



Supplementary Information References

- Agee, C.B., Wilson, N.V., McCubbin, F.M., Ziegler, K., Polyak, V.J., Sharp, Z.D., Asmerom, Y., Nunn, M.H., Shaheen, R., Thiemens, M.H., Steele, A., Fogel, M.L., Bowden, R., Glamoclija, M., Zhang, Z., Elardo, S.M. (2013) Unique Meteorite from Early Amazonian Mars: Water-Rich Basaltic Breccia Northwest Africa 7034. *Science* 339, 780-785. <https://doi.org/10.1126/science.1228858>
- Baron, F., Gaudin, A., Lorand, J.-P., Mangold, N. (2019) New Constraints on Early Mars Weathering Conditions From an Experimental Approach on Crust Simulants. *Journal of Geophysical Research: Planets* 124, 1783-1801. <https://doi.org/10.1029/2019JE005920>
- Cánneva, A., Giordana, I.S., Erra, G., Calvo, A. (2017) Organic Matter Characterization of Shale Rock by X-ray Photoelectron Spectroscopy: Adventitious Carbon Contamination and Radiation Damage. *Energy & Fuels* 31, 10414-10419. <https://doi.org/10.1021/acs.energyfuels.7b01143>
- Dethlefsen, F., Haase, C., Ebert, M., Dahmke, A. (2012) Uncertainties of geochemical modeling during CO₂ sequestration applying batch equilibrium calculations. *Environmental Earth Sciences* 65, 1105-1117. <https://doi.org/10.1007/s12665-011-1360-x>
- Fairley, N., Fernandez, V., Richard-Plouet, M., Guillot-Deudon, C., Walton, J., Smith, E., Flahaut, D., Greiner, M., Biesinger, M., Tougaard, S., Morgan, D., Baltrusaitis, J. (2021) Systematic and collaborative approach to problem solving using X-ray photoelectron spectroscopy. *Applied Surface Science Advances* 5, 100112. <https://doi.org/10.1016/j.apsadv.2021.100112>
- Gago-Duport, L., Briones, M., Rodríguez, J.B., Covelo, B. (2008) Amorphous calcium carbonate biomineralization in the earthworm's calciferous gland: Pathways to the formation of crystalline phases. *Journal of Structural Biology* 162, 422-435. <https://doi.org/10.1016/j.jsb.2008.02.007>
- Hewins, R.H., Zanda, B., Humayun, M., Nemchin, A., Lorand, J.-P., Pont, S., Deldicque, D., Bellucci, J.J., Beck, P., Leroux, H., Marinova, M., Remusat, L., Göpel, C., Lewin, E., Grange, M., Kennedy, A., Whitehouse, M.J. (2017) Regolith breccia Northwest Africa 7533: Mineralogy and petrology with implications for early Mars. *Meteoritics & Planetary Science* 52, 89-124. <https://doi.org/10.1111/maps.12740>
- Humayun, M., Nemchin, A., Zanda, B., Hewins, R.H., Grange, M., Kennedy, A., Lorand, J.P., Göpel, C., Fieni, C., Pont, S., Deldicque, D. (2013) Origin and age of the earliest Martian crust from meteorite NWA 7533. *Nature* 503, 513-516. <https://doi.org/10.1038/nature12764>
- Jiang, C.Z., Tosca, N.J. (2020) Growth kinetics of siderite at 298.15 K and 1 bar. *Geochimica et Cosmochimica Acta* 274, 97-117. <https://doi.org/10.1016/j.gca.2020.01.047>
- Jones, G.C., Jackson, B. (1993) *Infrared Transmission Spectra of Carbonate Minerals*. Springer, Dordrecht. <https://doi.org/10.1007/978-94-011-2120-0>
- Kissick, L.E., Mather, T.A., Tosca, N.J. (2021) Unravelling surface and subsurface carbon sinks within the early Martian crust. *Earth and Planetary Science Letters* 557, 116663. <https://doi.org/10.1016/j.epsl.2020.116663>
- Kloprogge, T., Wood, B. (2020) *Handbook of Mineral Spectroscopy Volume 1 X-ray Photoelectron Spectra*. In: Kloprogge, J.T. and Wood, B.J. (Eds.) Elsevier, Amsterdam (Netherlands), Oxford (UK), Cambridge (USA). <https://doi.org/10.1016/B978-0-12-804522-0.00001-8>
- Le Bas, M.J., Le Maitre, R.W., Streckeisen, A., Zanettin, B. (1986) A Chemical Classification of Volcanic Rocks Based on the Total Alkali-Silica Diagram. *Journal of Petrology* 27, 745-750. <https://doi.org/10.1093/petrology/27.3.745>
- Lu, P., Fu, Q., Seyfried, W.E., Hedges, S.W., Soong, Y., Jones, K., Zhu, C. (2013) Coupled alkali feldspar dissolution and secondary mineral precipitation in batch systems – 2: New experiments with supercritical CO₂ and implications for carbon sequestration. *Applied Geochemistry* 30, 75-90. <https://doi.org/10.1016/j.apgeochem.2012.04.005>
- Mangold, N., Thompson, L.M., Forni, O., Williams, A.J., Fabre, C., Le Deit, L., Wiens, R.C., Williams, R., Anderson, R.B., Blaney, D.L., Calef, F., Cousin, A., Clegg, S.M., Dromart, G., Dietrich, W.E., Edgett, K.S., Fisk, M.R., Gasnault, O., Gellert, R., Grotzinger, J.P., Kah, L., Le Mouélic, S., McLennan, S.M., Maurice, S., Meslin, P.-Y., Newsom, H.E., Palucis, M.C., Rapin, W., Sautter, V., Siebach, K.L., Stack, K., Sumner, D., Yingst, A. (2016) Composition of conglomerates analyzed by the Curiosity rover: Implications for Gale Crater crust and sediment sources. *Journal of Geophysical Research: Planets* 121, 353-387. <https://doi.org/10.1002/2015JE004977>



- Montes-Hernandez, G., Renard, F. (2016) Time-Resolved in Situ Raman Spectroscopy of the Nucleation and Growth of Siderite, Magnesite, and Calcite and Their Precursors. *Crystal Growth & Design* 16, 7218-7230. <https://doi.org/10.1021/acs.cgd.6b01406>
- Morrison, S.M., Downs, R.T., Blake, D.F., Vaniman, D.T., Ming, D.W., Hazen, R.M., Treiman, A.H., Achilles, C.N., Yen, A.S., Morris, R.V., Rampe, E.B., Bristow, T.F., Chipera, S.J., Sarrazin, P.C., Gellert, R., Fendrich, K.V., Morookian, J.M., Farmer, J.D., Des Marais, D.J., Craig, P.I. (2018) Crystal chemistry of martian minerals from Bradbury Landing through Naukluft Plateau, Gale crater, Mars. *American Mineralogist* 103, 857-871. <https://doi.org/10.2138/am-2018-6124>
- Nielsen, M.R., Sand, K.K., Rodriguez-Blanco, J.D., Bovet, N., Generosi, J., Dalby, K.N., Stipp, S.L.S. (2016) Inhibition of Calcite Growth: Combined Effects of Mg²⁺ and SO₄²⁻. *Crystal Growth & Design* 16, 6199-6207. <https://doi.org/10.1021/acs.cgd.6b00536>
- Parkhurst, D.L., Apello, C.A. (2014) Description of Input and Examples for Phreeqc Version 3: A Computer Program for Speciation, Batch-reaction, One-dimensional Transport, and Inverse Geochemical Calculations. *Techniques and Methods*, Reston, VA. <https://doi.org/10.3133/tm6A43>
- Payne, B.P., Biesinger, M.C., McIntyre, N.S. (2011) X-ray photoelectron spectroscopy studies of reactions on chromium metal and chromium oxide surfaces. *Journal of Electron Spectroscopy and Related Phenomena* 184, 29-37. <https://doi.org/10.1016/j.elspec.2010.12.001>
- Teng, H.H., Dove, P.M., De Yoreo, J.J. (2000) Kinetics of calcite growth: surface processes and relationships to macroscopic rate laws. *Geochimica et Cosmochimica Acta* 64, 2255-2266. [https://doi.org/10.1016/S0016-7037\(00\)00341-0](https://doi.org/10.1016/S0016-7037(00)00341-0)
- Zhu, C., Lu, P. (2009) Alkali feldspar dissolution and secondary mineral precipitation in batch systems: 3. Saturation states of product minerals and reaction paths. *Geochimica et Cosmochimica Acta* 73, 3171-3200. <https://doi.org/10.1016/j.gca.2009.03.015>

